



# Unravelling the effect of $\text{Cl}^-$ on alkaline saline water electrooxidation on NiFe (oxy)hydroxides

Feng Dong<sup>a</sup>, Huan Duan<sup>a</sup>, Zedong Lin<sup>a,b</sup>, Haifeng Yuan<sup>a</sup>, Min Ju<sup>a</sup>, Xinjuan Du<sup>a</sup>, Jinqiang Gao<sup>a</sup>, Jun Yu<sup>a,\*</sup>, Shihe Yang<sup>a,b,\*\*</sup>

<sup>a</sup> Guangdong Key Laboratory of Nano-Micro Material Research, School of Chemical Biology and Biotechnology, Peking University Shenzhen Graduate School, Shenzhen 518055, PR China

<sup>b</sup> Institute of Biomedical Engineering, Shenzhen Bay Laboratory, Shenzhen 518107, PR China

## ARTICLE INFO

### Keywords:

OER  
 $\text{Cl}^-$  effect  
 High-valence Ni(IV)  
 FTacV  
 $\text{OH}^*$  deprotonation step

## ABSTRACT

One of the major problems for seawater electrolysis is chloride corrosion arising from the chlorine oxidation reaction (ClOR). Although researchers have endeavored to improve the OER activity (overpotentials below 490 mV) to avoid the ClOR, an OER deactivation effect of chloride anions still looms large even before the ClOR becomes a serious issue, and its mechanism remains unclear. Herein using a simple Fourier transform ac voltammetry (FTacV) method, we unveil a hidden fact about the detrimental effect of  $\text{Cl}^-$  over an exemplar catalyst NiFe (oxy)hydroxide: it increases the formation potential of Ni(IV) thus lowering the OER performance. This is borne out by theoretical calculations, which reveal changes in the electronic environment of Ni sites induced by replacing the bridge  $\text{OH}^-$  species with  $\text{Cl}^-$  and the resulting difficulty to form high-valence Ni(IV). The consequence is a large increase in energy barrier of the  $\text{OH}^*$  deprotonation step that lowers the OER activity. The poison effect of  $\text{Cl}^-$  can be restrained by adding carbonate ions, which restores the facile formation of Ni(IV) and stabilizes the electrode for over 140-h saline water oxidation reaction at the current density of  $100 \text{ mA cm}^{-2}$ . This work helps to guide the design of active and durable seawater-splitting electrocatalysts.

## 1. Introduction

Electrocatalytic water splitting plays a significant role in green hydrogen production by using sustainable electricity [1,2]. The oxygen evolution reaction (OER) at the anode involves a sluggish four-electron transfer process, which hinders the kinetics of the whole water splitting reaction [3–9]. In alkaline environment, Ni-based (oxy)hydroxides have shown good OER activities, especially the NiFe (oxy)hydroxides [10–15]. Since Trotochaud and Young et al. revealed that the absorption of trace Fe impurities could make a big difference to the activity of Ni  $(\text{OH})_2/\text{NiOOH}$  [16], more researches have ascribed the high OER activity of NiFe catalysts to the synergy interaction between Ni and Fe [17]. To further discern the real OER active sites of NiFe catalysts, many researchers have performed the operando spectroscopy to directly observe the chemical structure of metal ions during OER. Numerous Near-edge X-ray absorption spectroscopy (XAS) measurements verify the generation of highly oxidized Ni centers ( $>3+$ ) during the OER

process [17–22]. Inspired by this, our group and other researchers began to synthesize catalysts containing high-valence Ni directly, which has shown excellent OER performance [23,24].

FTacV (Fourier transformed ac voltammetry) has been employed as a powerful tool for unraveling intricate electrochemical mechanisms as it's insensitive to the catalytic processes and other capacitive processes such that electron transfer reactions can be differentiated from non-Faradaic reactions [25–27]. The mechanisms of water electrooxidation catalyzed by  $\text{Co}(\text{OH})_2$  and  $\text{Ni}(\text{OH})_2$  were studied by FTacV. In this case,  $\text{CoO}_2$  was formed at 0.71 V vs. Ag/AgCl and  $\text{NiOOH}$  was formed at 0.39 V vs. Ag/AgCl, but without generating Ni(IV) [28]. The FTacV method has been further proved to be effective for the study of OER process of transition metal oxides including  $\text{CoO}_x$ ,  $\text{MnO}_x$  and  $\text{NiO}_x$  [29].

Direct electrolysis of seawater is considered a more energy conserving strategy for clean hydrogen generation than that of pure water [30,31]. The alkaline system for seawater electrolysis can achieve nearly 100% OER selectivity as long as the overpotential of the catalyst

\* Corresponding author.

\*\* Corresponding author at: Guangdong Key Laboratory of Nano-Micro Material Research, School of Chemical Biology and Biotechnology, Peking University Shenzhen Graduate School, Shenzhen 518055, PR China.

E-mail addresses: [yujun@szu.edu.cn](mailto:yujun@szu.edu.cn) (J. Yu), [chsyang@pku.edu.cn](mailto:chsyang@pku.edu.cn) (S. Yang).

<https://doi.org/10.1016/j.apcatb.2023.123242>

Received 25 June 2023; Received in revised form 24 August 2023; Accepted 28 August 2023

Available online 29 August 2023

0926-3373/© 2023 Elsevier B.V. All rights reserved.

is lower than the standard potential difference ( $\sim 490$  mV) between the OER and the chlorine oxidation reaction (ClOR) [32]. However, the OER performance in seawater splitting was found to deteriorate even when the ClOR does not occur [33,34]. Such a negative effect of OER deactivation induced by the chloride anions has eluded understanding until now.

In this work, we employ FTacV to unravel the catalytic center and the effect of chlorine anions on the center of a prototypical OER catalyst NiFe (oxy)hydroxide. The  $\text{Ni}_v(\text{OH})_2/\text{FeOOH}$  catalyst was synthesized by forming FeOOH nanoparticles on the surface of  $\text{Ni}_v(\text{OH})_2$  nanosheets, concurrent with generation of the high-valence Ni(IV) with excellent OER activity. The formation of Ni(IV), which lowered the overpotential to only 262 mV at the large current density of  $100 \text{ mA cm}^{-2}$ , was promoted by the surficial FeOOH. Surprisingly, the formation potential of Ni(IV) is increased with increasing chlorine anions, leading to OER performance decay. Density functional theory (DFT) calculations showed that the incorporation of Cl-Cl changes the electronic environment of Ni sites and increases the energy barrier in the  $\text{OH}^*$  deprotonation step, thus lowering the OER activity. By adding carbonate ions, the OER activity of  $\text{Ni}_v(\text{OH})_2/\text{FeOOH}$  could be recovered and a long-term stability of over 140 h at the current density of  $100 \text{ mA cm}^{-2}$  in saline water was achieved.

## 2. Experimental section

### 2.1. Preparation of $\text{Ni}_v(\text{OH})_2$

$\text{Ni}_v(\text{OH})_2$  were directly synthesized on nickel foam following the method mentioned in previous work of our group [35].

### 2.2. Preparation of $\text{Ni}_v(\text{OH})_2/\text{FeOOH}$

$\text{Ni}_v(\text{OH})_2/\text{FeOOH}$  was prepared by immersing the sample (about  $1 \times 2 \text{ cm}$ ) in 20 ml of 0.01 M  $\text{FeSO}_4 \cdot 7 \text{ H}_2\text{O}$  aqueous solution for 60 min. Then the  $\text{Ni}_v(\text{OH})_2/\text{FeOOH}$  was washed with DI water/ethanol three times and dried at room temperature.

### 2.3. Preparation of $\text{RuO}_2/\text{NF}$

$\text{RuO}_2/\text{NF}$  was prepared by dispersing 2 mg  $\text{RuO}_2$  powder in 400  $\mu\text{L}$  ethanol and then sonicating for 30 min. Subsequently, 400  $\mu\text{L}$  polytetrafluoroethylene (PTFE) water suspension (4 wt%) was added in to  $\text{RuO}_2$  suspension sonicating for 30 min to form a catalyst ink. The catalyst ink was uniformly drop-casted on nickel foam with a mass loading of  $\sim 2 \text{ mg/cm}^2$  to prepare working electrodes.

### 2.4. Materials characterization

All the catalyst samples were characterized by scanning electron microscopy (SEM, JSM-7800 F) at 5.0 kV. The crystal structure of samples was determined by X-ray diffraction (XRD, D8 Advance X-ray diffractometer) operated at 40 kV and 40 mA with a  $\text{Cu K}\alpha$  radiation ( $\lambda = 1.5405 \text{ \AA}$ ) in the  $2\theta$  ranging from  $5^\circ$  to  $80^\circ$  with a step size of  $0.02^\circ$ . Transmission Electron Microscopy and electron diffraction pattern (ED pattern) were collected on JEM-3200FS. High resolution TEM (HRTEM), high-angle annular dark-field (HAADF) image and the energy dispersive X-ray Spectroscopy (EDS) were performed on FEI talos F200x G2. The samples were made by sonicating the catalysts off from the nickel foam, then the suspensions with catalyst were dropped onto the copper grid for TEM and following characterization. X-ray photoelectron spectroscopy (XPS) spectra were collected on ESCALAB 250XI (ThermoScientific). Spectra were analyzed using XPSPEAK software. The C1s peak for adventitious hydrocarbons at 284.6 eV was used for binding energy calibration. The ratio of Ni/Fe was examined by Inductively coupled plasma-atomic emission spectroscopy (ICP-AES, JY2000-2).

### 2.5. Electrochemical measurements

Electrochemical measurements were carried out in a standard three electrode system conducted by a CHI 760E electrochemistry workstation. The as-prepared freestanding catalysts@Ni foam were used as the working electrode, platinum flat ( $1 \times 1 \text{ cm}$ ) and Hg/HgO electrode were used as the counter and reference electrode, respectively. The acquired electrochemical data were referred to reversible hydrogen electrode (RHE) scale by following equation:

$$E (\text{V vs-RHE}) = E (\text{V vs-Hg/HgO}) + 0.0977 \text{ V} + 0.0592 \times \text{pH}$$

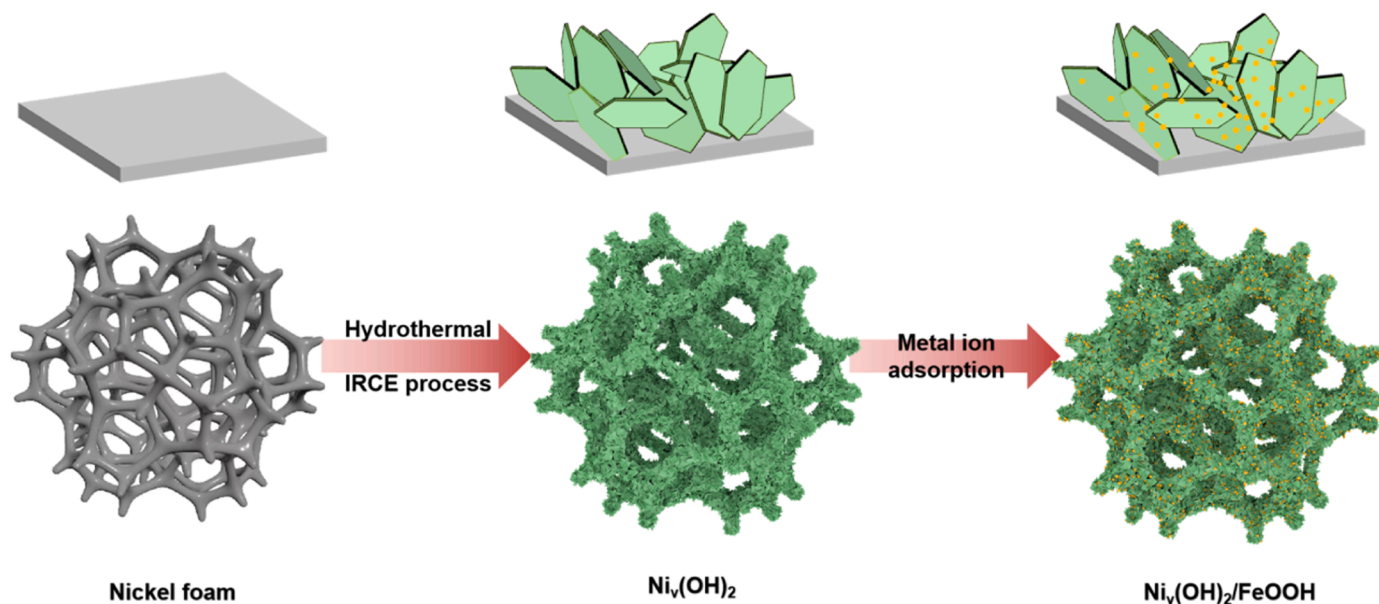
All measurements were carried out in 1 M KOH. The cyclic voltammetry (CV) measurements were cycled at a scan rate of  $10 \text{ mV s}^{-1}$  for 30 times in the potential range from 1.22 to 1.53 V vs. RHE until a stable CV curve was achieved before collecting polarization curves and Tafel plots of the catalysts. Linear sweep voltammetry (LSV) was carried out at  $2 \text{ mV s}^{-1}$  for the polarization curves and  $0.5 \text{ mV s}^{-1}$  for Tafel plots. Electrochemical impedance spectroscopy (EIS) analysis were conducted at 1.53 V vs RHE at overpotential of 300 mV at DC potential of 5 mV with the frequency ranging from 100 kHz to 0.1 Hz.  $iR$  compensation of LSV polarization curves were corrected manually with the value of solution resistance that required from the Nyquist plot of impedance spectra. CV measurements for electrochemically active surface area (ECSA) were performed in the potential range from 1.02 to 1.12 V vs. RHE at different scan rates of 10, 20, 30, 40, 50  $\text{mV s}^{-1}$ , and 20 cycles were recorded. The ECSA of different electrodes was calculated from the CV curves. The stability was tested at constant current densities of 50, 100, 200  $\text{mA cm}^{-2}$ . Fourier Transformed alternating current voltametric (FTacV) experiments were carried out using FTacV technique equipped in CHI 760E with an amplitude ( $\Delta E$ ) of 80 mV and a frequency ( $f$ ) of 0.512 Hz.

In order to figure out the effect of chloride anions on  $\text{Ni}_v(\text{OH})_2/\text{FeOOH}$ , electrolytes containing various concentration of chloride anion were prepared by adding sodium chloride into 1 M KOH to get 1 M KOH/0.5 M NaCl, 1 M KOH/1 M NaCl, 1 M KOH/2 M NaCl solutions. To calculate the  $\text{O}_2$  generation Faradaic efficiency in 1 M KOH and 1 M KOH/2 M NaCl solutions, the oxygen generated in anode of H-cell was quantitatively analyzed by gas chromatography (GC, SHIMADZU GC-2014). A thermal conductivity detector (TCD) was used to quantify oxygen ( $\text{O}_2$ ). Throughout the testing process, high purity nitrogen (99.9999%) was used as the carrier gas for the GC. Before the GC started to test, each potential should be kept running for 10 min to remove the residual gas in the equipment at the current working potential.

### 2.6. Model and computational detail

All DFT calculations were performed using the Vienna ab initio simulation package (VASP) [36,37]. The projector-augmented-wave (PAW) method is employed to describe the core-valence interactions. Perdew-Burke-Ernzerhof (PBE) generalized gradient approximation (GGA) was adopted to treat the exchange correlation functional [38,39]. To describe the localization of the 3d electrons, the Hubbard effective terms are fixed as 6.6 eV for Ni and 3.5 eV for Fe [40]. To account for the weak dispersion interactions, these functionals were used in combination with the Grimme's correction scheme (DFT-D3) [41]. The plane wave energy cutoff was set to 500 eV. The energy convergence criterion is set as  $1 \times 10^{-4} \text{ eV}$ . For structural optimizations, the force convergence criterion is set as  $0.02 \text{ eV \AA}^{-1}$ . A Monkhorst-Pack k-point grid of  $3 \times 3 \times 1$  is chosen to sample the reciprocal space for the calculation systems [42].

The  $\beta\text{-NiOOH}$  (11 $\bar{2}$ 0) surface was built by a bisecting cleavage along two Ni-O bonds per Ni. As a result, the exposed Ni atoms were coordinated to only four lattice O, which was determined from HR-TEM measurements. Fe dopants were inserted afterward by partial substitution of Ni atoms with uniform distribution. Cl atoms would follow two different models, attaching to the external Ni ones or substituting the



**Scheme 1.** Schematic illustration of the synthetic route of  $\text{Ni}_v(\text{OH})_2/\text{FeOOH}$ .

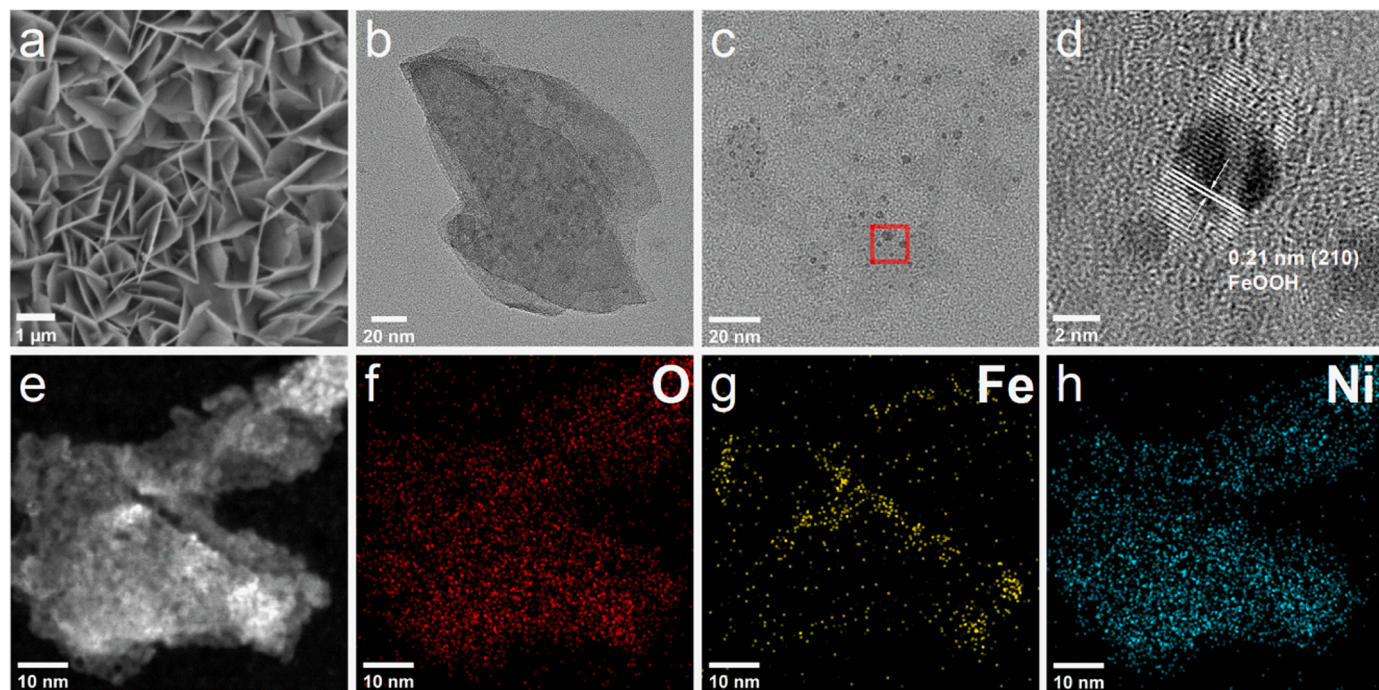


**Fig. 1.** (a) SEM, (b, c) TEM and (d) HR-TEM images of  $\text{Ni}_v(\text{OH})_2/\text{FeOOH}$ . (e) The HAADF-STEM image and the corresponding EDS mapping of (f) O, (g) Fe and (h) Ni element of  $\text{Ni}_v(\text{OH})_2/\text{FeOOH}$ .

-OH groups with 25% of the surface coverage. A vacuum layer of at least 15 Å thickness was added into the built supercell to avoid the interaction between top and bottom surfaces.

Based on the computational hydrogen electrode models, the free energy of  $\text{OH}^-$  can be expressed as  $G(\text{OH}^-) = G(\text{H}_2\text{O}) - G(\text{H}^+)$  assuming the equilibrium process  $\text{H}^+ + \text{OH}^- \rightarrow \text{H}_2\text{O}$ , where the  $G(\text{H}^+)$  is equal of the free energy of  $\frac{1}{2} \text{H}_2$ . The adsorption energy of intermediates was calculated by using the relationship  $\Delta E_{\text{adsorption}} = E_{\text{system}} - E_{\text{slab}} - E_{\text{adsorbates}}$ , and then converting into Gibbs free energy with the equation  $\Delta G = \Delta E - T \cdot \Delta S + \Delta \text{ZPE}$ . Entropy changes ( $\Delta S$ ) were obtained from tabulated values (webbook.nist.gov/chemistry/). Zero-point energies ( $\Delta \text{ZPE}$ ) were taken from the J. K. Nørskov's prior work [43].

### 3. Results and discussion

#### 3.1. Morphology and structure characterizations

The schematic illustration for the synthesis of  $\text{Ni}_v(\text{OH})_2/\text{FeOOH}$  is shown in Scheme 1.  $\text{Ni}_v(\text{OH})_2$  with Ni vacancies was firstly synthesized through hydrothermal process followed by ionic reductive complexation extraction (IRCE) process according to our reported work [35]. Then the  $\text{Ni}_v(\text{OH})_2$  sample was immersed in Fe(II) instead of Fe(III) aqueous solution to obtain  $\text{Ni}_v(\text{OH})_2/\text{FeOOH}$ . The pH of the Fe(II) aqueous solution is less acidic so that not to destroy the as-prepared  $\text{Ni}_v(\text{OH})_2$  nanosheets (Fig. S1). The SEM image of  $\text{Ni}_v(\text{OH})_2/\text{FeOOH}$  is shown in Fig. 1a, and

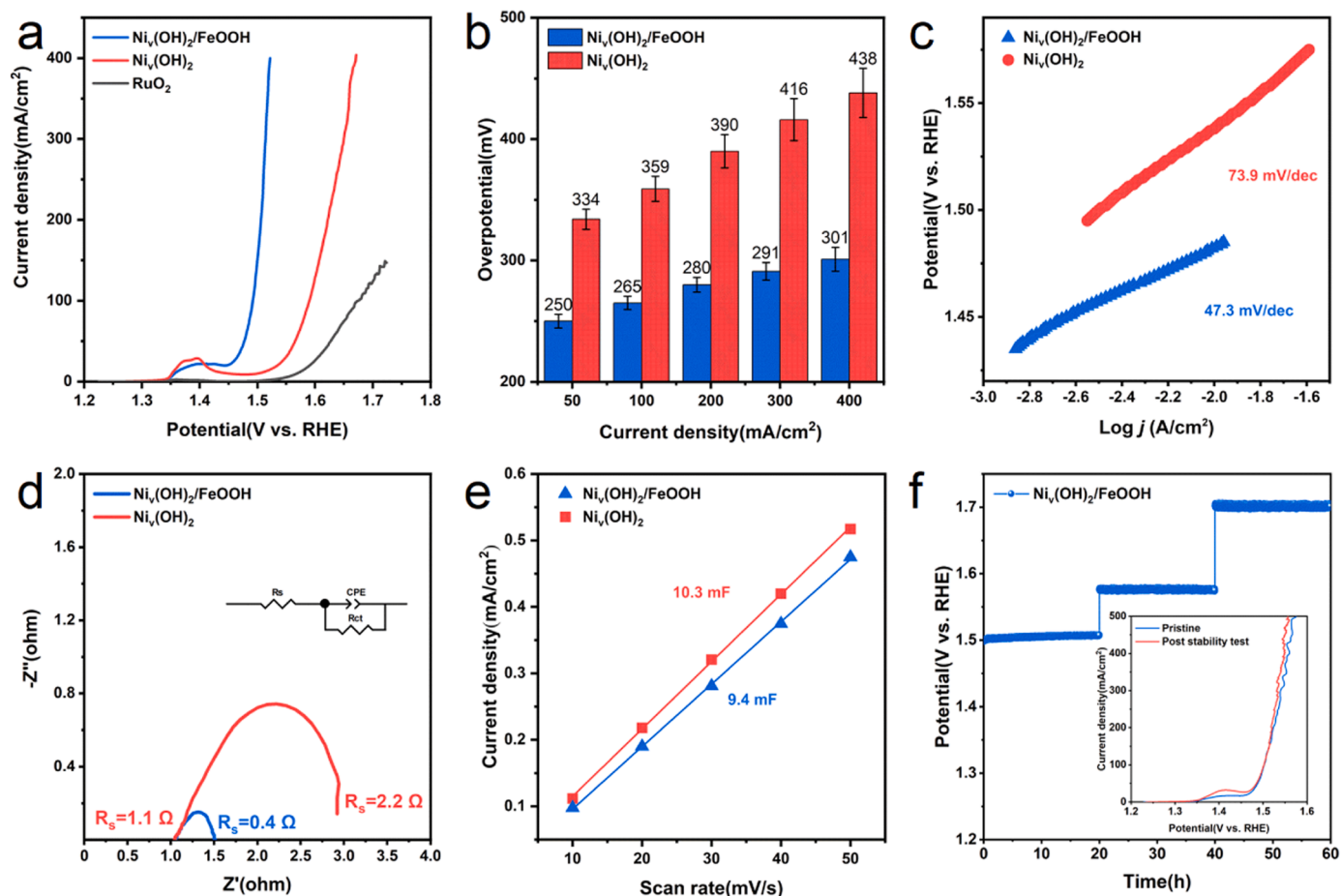


**Fig. 2.** (a) LSV curves of  $\text{RuO}_2$ ,  $\text{Ni}_x(\text{OH})_2$  and  $\text{Ni}_x(\text{OH})_2/\text{FeOOH}$  ( $iR$ -corrected) measured in 1 M KOH. (b) Overpotential comparison of  $\text{Ni}_x(\text{OH})_2$  and  $\text{Ni}_x(\text{OH})_2/\text{FeOOH}$  at different current densities. (c) Tafel plots, (d) Nyquist plots, and (e) current density at OCP as a function of scan rate for  $\text{Ni}_x(\text{OH})_2$  and  $\text{Ni}_x(\text{OH})_2/\text{FeOOH}$ . (f) Chronopotentiometry curves of  $\text{Ni}_x(\text{OH})_2/\text{FeOOH}$  tested at the current density of 50  $\text{mA}/\text{cm}^2$ , 100  $\text{mA}/\text{cm}^2$  and 200  $\text{mA}/\text{cm}^2$  (inset: LSV curves before and after stability testing).

the morphology remains nanosheet as that of  $\text{Ni}_x(\text{OH})_2$ . The transmission electron microscopy (TEM) images (Fig. 1b) also displayed the nanosheet structure of  $\text{Ni}_x(\text{OH})_2/\text{FeOOH}$ , and the lattice plane of (100) ascribed to  $\beta\text{-Ni}(\text{OH})_2$  and the lattice plane of (200) ascribed to FeOOH were observed, respectively (Fig. S2). As shown in Fig. 1c, multitudinous brunette nanodots were uniformly distributed on the surface of the nanosheets, which were proved to be FeOOH nanoparticles with a size of less than 5 nm (Fig. 1d). The high-angle annular dark-field (HAADF) image of  $\text{Ni}_x(\text{OH})_2/\text{FeOOH}$  in Fig. S3 also displays bright FeOOH nanodots and dark  $\text{Ni}_x(\text{OH})_2$  nanosheets substrate clearly. The HAADF-STEM EDS images (Fig. 1f, h) reveal the uniform distribution of O and Ni elements in  $\text{Ni}_x(\text{OH})_2/\text{FeOOH}$ . The distribution of Fe element presents partial aggregation, which together corroborates the nanoparticle morphology of FeOOH (Fig. 1g). Inductively coupled plasma-atomic emission spectroscopy (ICP-AES) analysis reveals that the molar ratio of Ni/Fe in  $\text{Ni}_x(\text{OH})_2/\text{FeOOH}$  was about 16:1 as shown in Table S1.

The X-ray diffraction (XRD) patterns of  $\text{Ni}_x(\text{OH})_2$  and  $\text{Ni}_x(\text{OH})_2/\text{FeOOH}$  are shown in Fig. S4, and the peaks located at  $19^\circ$ ,  $33^\circ$ ,  $39^\circ$ ,  $52^\circ$  and  $59^\circ$  are ascribed to  $\beta\text{-Ni}(\text{OH})_2$  (PDF-#03-0177), consistent with the TEM results. No peaks ascribed to FeOOH were observed for  $\text{Ni}_x(\text{OH})_2/\text{FeOOH}$  because of the low content and uniform distribution of surface FeOOH nanoparticles. The Fe 2p XPS spectrum of  $\text{Ni}_x(\text{OH})_2/\text{FeOOH}$  is shown in Fig. S5. The obvious noisy signals also indicate the low content of Fe. Two peaks at 710.3 and 724 eV can be assigned to Fe 2p<sub>3/2</sub> and Fe 2p<sub>1/2</sub> of FeOOH, respectively. The peaks with binding energy values of 713 and 727.5 eV can be ascribed to the shakeup satellite peaks of

FeOOH. The above results revealed that FeOOH nanoparticles were formed on the surface of  $\text{Ni}_x(\text{OH})_2$  nanosheet in  $\text{Ni}_x(\text{OH})_2/\text{FeOOH}$ .

### 3.2. Electrocatalytic activities

The OER electrochemical performances of catalysts were evaluated in 1.0 M KOH electrolyte using a typical three-electrode system. From the linear sweep voltammetry (LSV) curves with  $iR$  compensation (Fig. 2a),  $\text{Ni}_x(\text{OH})_2/\text{FeOOH}$  showed the highest catalytic activity with an overpotential of 212 mV at 10  $\text{mA}/\text{cm}^2$ , which is remarkably lower than that of  $\text{Ni}_x(\text{OH})_2$  and  $\text{RuO}_2$ . There is a broad pre-oxidation peak around 1.4 V for  $\text{Ni}_x(\text{OH})_2/\text{FeOOH}$ , which results from the different phases of nickel hydroxide, including  $\alpha$ -hydroxide and  $\beta$ -hydroxide, which are oxidized to trivalent nickel oxyhydroxide at the partially overlapped potentials. A variety of phase transformations could occur between different nickel hydroxide variants during the electrochemical activation process [44]. Moreover, as shown in Fig. 2b, for high current densities at 100, 200, 300 and 400  $\text{mA}/\text{cm}^2$ ,  $\text{Ni}_x(\text{OH})_2/\text{FeOOH}$  also delivered an excellent catalytic performance with low overpotential of 261, 276, 286, 294 mV, respectively. The OER activity of  $\text{Ni}_x(\text{OH})_2/\text{FeOOH}$  matched with up-to-date reported high-performance analogues for OER (Table S2). The reaction kinetics of  $\text{Ni}_x(\text{OH})_2$  and  $\text{Ni}_x(\text{OH})_2/\text{FeOOH}$  were evaluated by Tafel curves as presented in Fig. 2c.  $\text{Ni}_x(\text{OH})_2/\text{FeOOH}$  showed smaller Tafel slope of 47  $\text{mV}/\text{dec}^{-1}$  comparing with that of  $\text{Ni}_x(\text{OH})_2$  (74  $\text{mV}/\text{dec}^{-1}$ ), which indicating superb kinetic performance of  $\text{Ni}_x(\text{OH})_2/\text{FeOOH}$  [45–47]. Electrochemical impedance spectra (EIS) were also measured as shown in Fig. 2d. The

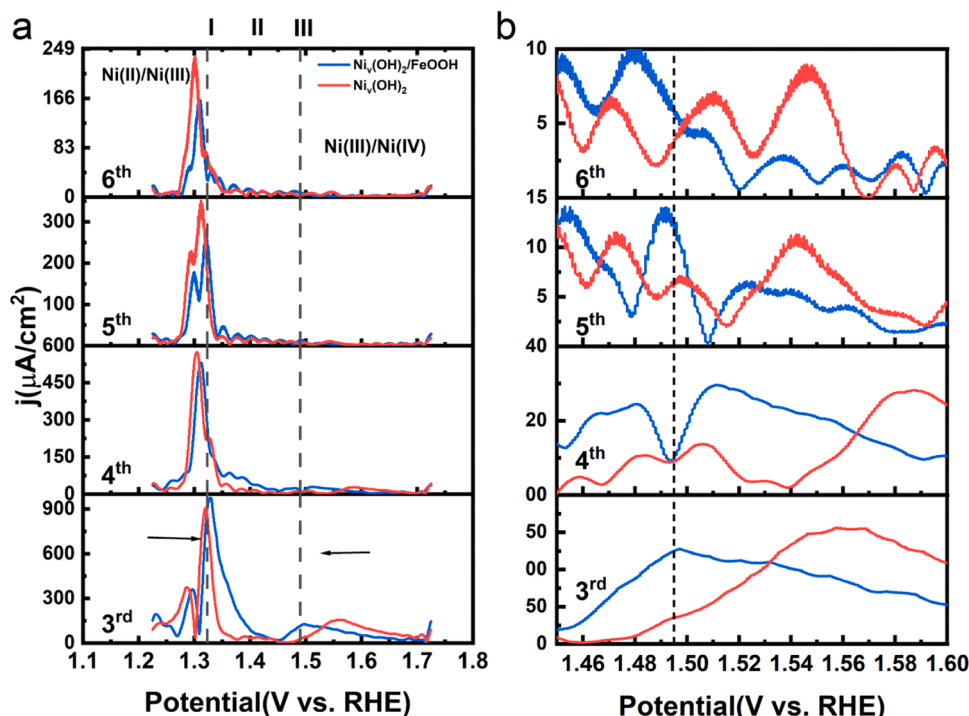


**Fig. 3.** (a) 3rd to 6th harmonic FTAC voltammetry components ( $f = 0.512$  Hz,  $\Delta E = 80$  mV, scan rate  $= 0.5$  mV s $^{-1}$ , positive sweep) for water oxidation catalyzed by  $\text{Ni}_v(\text{OH})_2$  (red line) and  $\text{Ni}_v(\text{OH})_2/\text{FeOOH}$  (blue line). (b) Enlarged region of a) on process III (dash line showing the potential causing faradaic reaction).

semicircle of EIS curve for  $\text{Ni}_v(\text{OH})_2/\text{FeOOH}$  was much smaller than that of  $\text{Ni}_v(\text{OH})_2$ , indicating a smaller charge transfer resistance [48,49]. As a result,  $\text{Ni}_v(\text{OH})_2/\text{FeOOH}$  showed favorable reaction kinetics for OER. The result of electrochemically active surface area (ECSA) measurements is shown in Fig. 2e.  $\text{Ni}_v(\text{OH})_2/\text{FeOOH}$  showed no larger ECSA than  $\text{Ni}_v(\text{OH})_2$ , which indicates that surface FeOOH did not enhance the amount of electrochemical active sites but the intrinsic activity of  $\text{Ni}_v(\text{OH})_2$ .

Stability is also a significant factor for evaluating the prospects of a catalyst. From Fig. 2f, it was obvious that the potentials for maintaining high current densities at 50 mA cm $^{-2}$ , 100 mA cm $^{-2}$  and 200 mA cm $^{-2}$  were negligibly changed for every 20 h. Moreover, comparing LSV curves between pristine sample and post-stability-test sample (Fig. 2f inset), the OER performance was even improved after stability test at 200 mA cm $^{-2}$ , which could be attributed to the increased activation Ni sites in inner structure. The post-stability-test sample also showed an enlarged pre-oxidized region related to the Ni(II)/Ni(III) redox confirming that more Ni sites participated in the reaction. Whereas the potential for the low current density of 50 mA cm $^{-2}$  increased obviously in only 10 h for sole  $\text{Ni}_v(\text{OH})_2$  as shown in Fig. S6.

### 3.3. High-valence Ni detection by FTacV

The high-valence Ni sites generated during OER process is considered as the active sites with high intrinsic activity. Numerous researchers have done Near-edge X-ray absorption spectroscopy (XAS) measurements to substantiate the generation of highly oxidized Ni centers ( $>3+$ ) during OER process [17–22]. While it is challenging to directly detect the Ni(III)/Ni(IV) redox transition using cyclic voltammetry due to the OER electrocatalytic wave, Fourier transformed alternating current voltammetry (FTacV) could be exploited to reveal the underlying electron transfer processes that are responsible for the OER under catalytic conditions. Our FTacV measurements used a large amplitude sinusoidal waveform with certain frequency superimposed on a linearly ramped potential. By analyzing the third and higher order harmonics which were devoid of background charging current and

insensitive to catalytic process [25–27], FTacV presents a new opportunity to detect the Ni(III)/Ni(IV) redox transition. From FTacV experiment of as-synthesized  $\text{Ni}_v(\text{OH})_2/\text{FeOOH}$  (Fig. 3a), the whole scanning region was clearly divided into three processes with response current value at  $\sim 1.33$  V (denoted as I), ca.  $1.35 - 1.45$  V (denoted as II) and  $\sim 1.49$  V (denoted as III). In process I, the electron transfer reaction was ascribed to Ni(II)/Ni(III) as the previous report [28]. The interpretation for process II was more complicated. A series of literature showed the similar observation at ca. 1.4 V and attributed it to the structural rearrangement [16,27,50–53]. When the potential was scanned to values in process III, intense oxygen evolution reaction was unequivocally observed, which suggested that process III related to water oxidation activity. Process III (enlarged region of process III as shown in Fig. 3b) was ascribed to Ni(III)/Ni(IV) redox transition on the basis of those literature that presented highly oxidized Ni centers ( $>3+$ ) under OER conditions, such as Ni-Fe(1.55 V) [54] and  $\text{Ni}_{0.75}\text{Fe}_{0.25}$ (1.72 V) [40]. The Ni(III)/Ni(IV) redox transition was detectable by evaluating FTacV measurements of  $\text{Ni}_v(\text{OH})_2/\text{FeOOH}$ . While no Ni(III)/Ni(IV) redox transition was observed for  $\text{Ni}_v(\text{OH})_2$ .

To further illustrate the promotion effect of FeOOH for the generation of Ni(IV) in  $\text{Ni}_v(\text{OH})_2/\text{FeOOH}$ , the  $\text{Ni}_v(\text{OH})_2/\text{FeOOH}$  sample was treated in 0.2 M KSCN solution to detach part of the surface FeOOH. From the Fe 2p XPS spectrum in Fig. S7, it is evident that the peak intensity of Fe decreases with increasing treatment time, indicating the detachment of surface FeOOH. As expected, the LSV curves in Fig. S8 show the same trend, pointing to the conclusion that the inferior electrochemical performance results from the lower Fe content. The FTacV measurement results of  $\text{Ni}_v(\text{OH})_2/\text{FeOOH}$  with different treatment time are shown in Fig. S9. As the treatment time was prolonged for  $\text{Ni}_v(\text{OH})_2/\text{FeOOH}$ , the potential of Ni(III)/Ni(IV) redox transition became more positive, indicating that an easier generation of Ni(IV) in  $\text{Ni}_v(\text{OH})_2/\text{FeOOH}$  was positively correlated with the OER performance.

To investigate the effect of chlorine anion concentration on OER performance, the  $\text{Ni}_v(\text{OH})_2/\text{FeOOH}$  catalyst was tested in 1 M KOH electrolyte solution containing various concentrations of sodium chloride, 0, 0.5 M, 1 M and 2 M. From the LSV curves with  $iR$  compensation

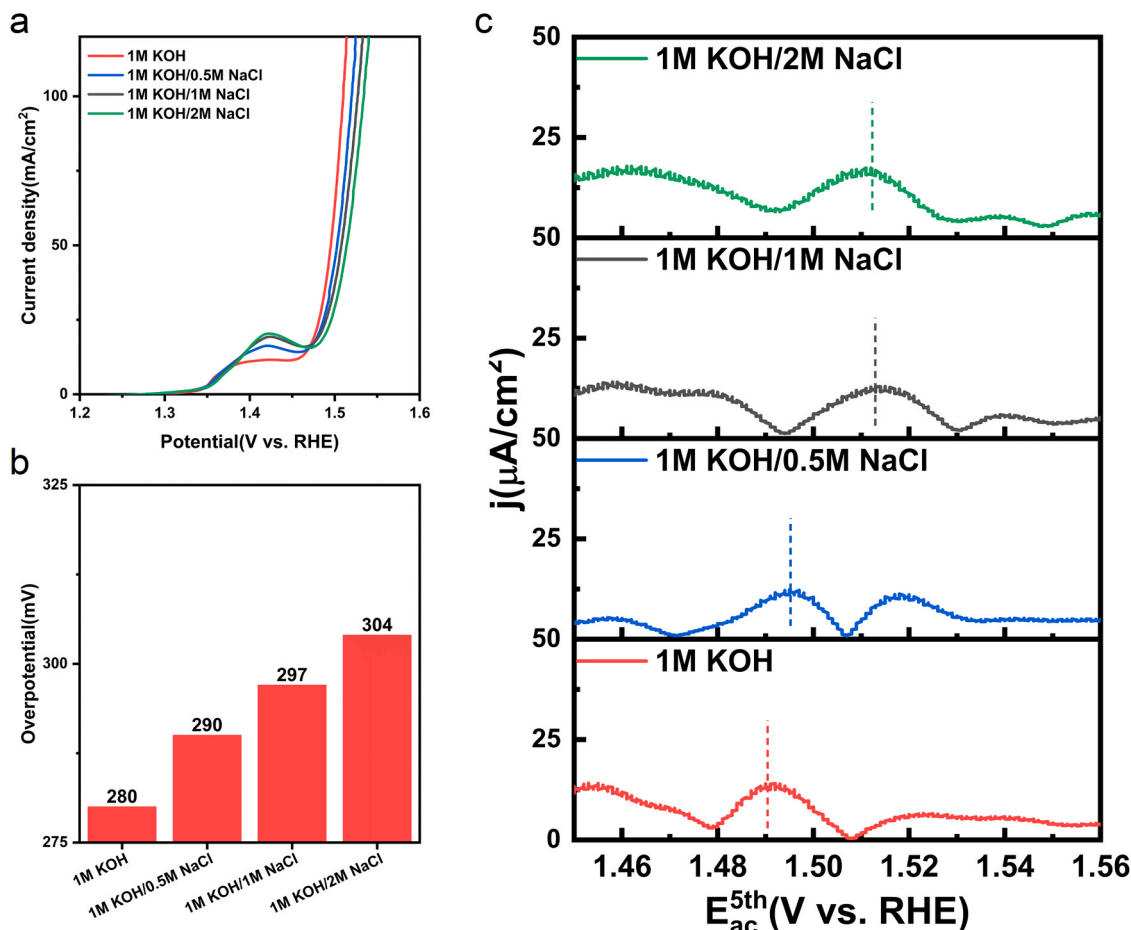


**Fig. 4.** (a) LSV curves of  $Ni(OH)_2/FeOOH$  (iR-corrected) tested in 1 M KOH electrolyte solution containing different concentrations of NaCl (0, 0.5 M, 1 M, 2 M). (b) Overpotential comparison of  $Ni(OH)_2/FeOOH$  measured in various electrolytes at  $100 \text{ mA cm}^{-2}$ . (c) 5th harmonic FTAC voltammetry components ( $f = 0.512 \text{ Hz}$ ,  $\Delta E = 80 \text{ mV}$ , scan rate  $= 0.5 \text{ mV s}^{-1}$ , positive sweep) of  $Ni(OH)_2/FeOOH$  process III measured in different electrolytes (dash lines indicating the potential of process III).

(Fig. 4a), it is clear that the OER performance became worse with the increase of the concentration of chlorine anion.  $Ni(OH)_2/FeOOH$  tested in 1 M KOH with 2 M NaCl showed the worst catalytic activity with an overpotential of 304 mV at  $100 \text{ mA cm}^{-2}$ , which is larger than the overpotential at  $100 \text{ mA cm}^{-2}$  measured in 1 M KOH by 24 mV (Fig. 4b). Fig. S10 and Fig. 4c show the FTACv measurement results of process III of  $Ni(OH)_2/FeOOH$  with different chlorine anion concentrations. The potential of  $Ni(III)/Ni(IV)$  redox transition becomes more positive for  $Ni(OH)_2/FeOOH$  with a higher chlorine anion concentration. It indicates that the existence of chlorine anion undermines the OER performance by hindering the generation of  $Ni(IV)$ . To rule out the possible corrosion of the substrate due to  $Cl^-$ , we conducted the following experiments. Specifically, ICP-MS of the electrolyte after different CV cycles (0th, 100th, 400th, 800th) in 1 M KOH/2 M NaCl was conducted (potential range from 1.22 to 1.62 V vs. RHE) to determine the content of Ni dissolved in the electrolyte. Before testing, the electrochemical activation was first cycled 20 times in 1 M KOH to reach steady curve. From the ICP results in Table S3, the Ni content dissolved in the electrolyte increases with the cycle times. It is gratifying that the amount of dissolved Ni was comparable to that from what was reported for NiFe-based catalysts in KOH, (pH  $\sim 14$ ) on the scale of ng/ml [55]. The CV curves of  $Ni(OH)_2/FeOOH$  have been shown in Fig. S11. Once a stable CV curve was achieved in 1 M KOH, the electrode was then cycled in 1 M KOH/2 M NaCl. On a close comparison of the CV curves in different electrolytes, one can see that the OER passivation effect of the chloride ions comes into play right from the first cycle and keeps steady afterwards under certain potential. A stability test has also been conducted shown in Fig. S12 to further illustrate the proper functioning of

the electrode in 1 M KOH/2 M NaCl. These results confirm that the OER performance degradation is not caused by  $Cl^-$ -induced substrate corrosion because if the nickel foam substrate was corroded by the chloride ions, the negative effect would have accumulated and shown continuous destructive effects of the catalysis activity. Meanwhile, the faradaic efficiencies for OER of  $Ni(OH)_2/FeOOH$  at 1.55 V, 1.6 V and 1.65 V are shown in Fig. S13, and in both KOH and KOH/2 M NaCl, they are nearly 100%, further confirming that the OER performance degradation of  $Ni(OH)_2/FeOOH$  in KOH/2 M NaCl is from the hindering generation of  $Ni(IV)$ . The high OER selectivity at the low potentials is understandable because the ClOR only occurs at the overpotentials above 490 mV (1.72 V vs RHE) [56].

### 3.4. Theoretical calculation

Density functional theory (DFT) calculations were performed to reveal the negative effects triggered by chloride anions and to further clarify the OER deactivation mechanism in simulated seawater. We selected the (11 $\bar{2}$ 0) surface (Fig. 5a), because it belongs to the family of surfaces that are exposed at the edge of catalyst sheets, and widely used to study the catalytic activity of layered materials [57].  $Cl^-$  is a non-reducible ligand and only store one oxidative charge over the entire potential window of the OER. The undercoordinated metal sites are favorable for the  $Cl^-$  coordination when the surface is in equilibrium with the electrolyte and in steady state. Two types of coordination form were designed and calculated: one is the  $Cl^-$  coordination between Ni and Fe denoted as  $Cl_B-(Fe)NiOOH$  (see Fig. 5a), and the other is the direct

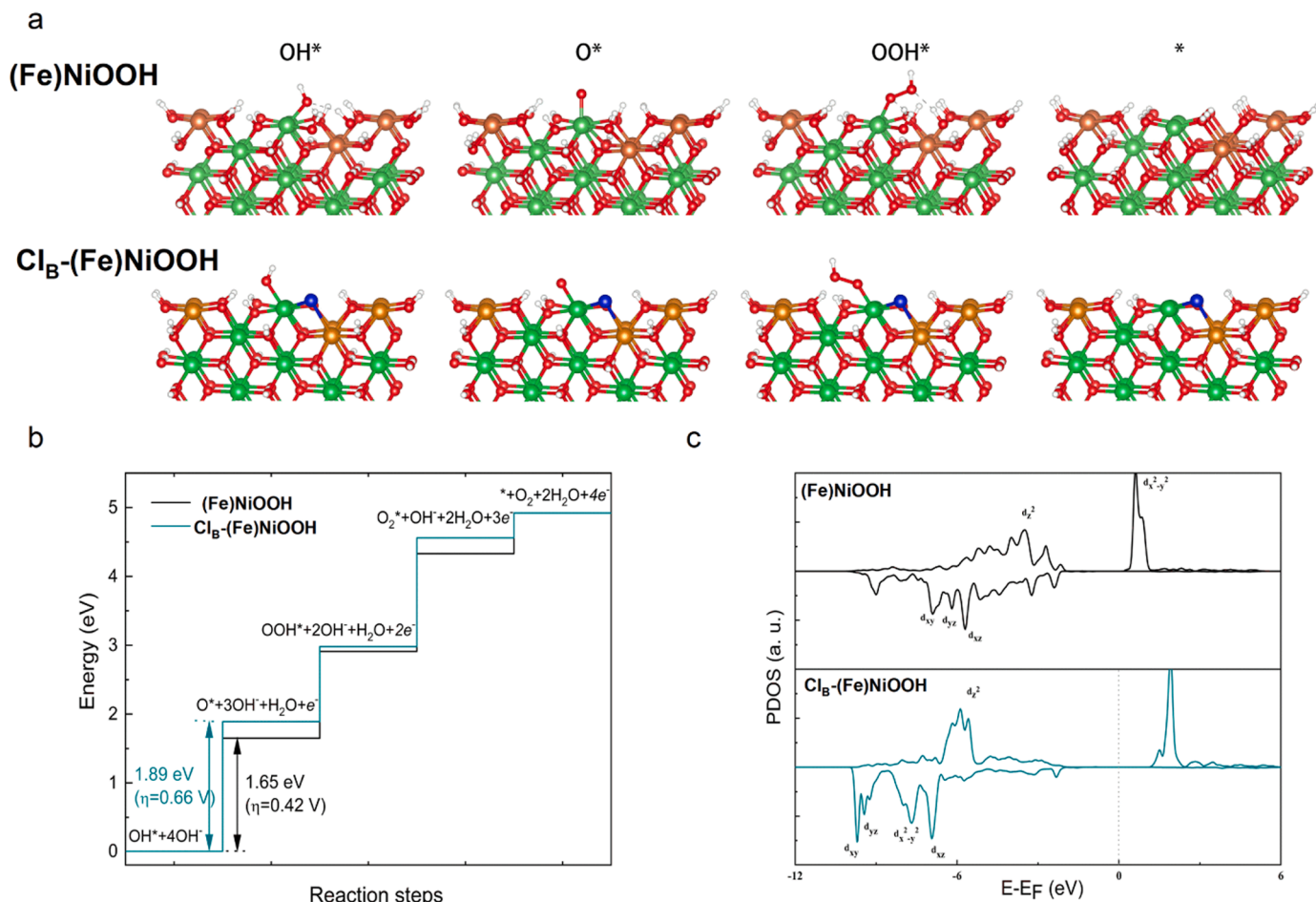


**Fig. 5.** (a) Ball-and-stick models illustrating the OER intermediates on the Ni-centered active sites. Color code for the atoms: white for hydrogen, red for oxygen, green for nickel, brown for iron, and blue for chlorine, respectively. (b) The energetic pathway of OER in the alkaline environment for (Fe)NiOOH and Cl<sub>B</sub>-(Fe)NiOOH. (c) The PDOS of active Ni sites.

coordination to the Ni site denoted as Cl<sub>N</sub>-(Fe)NiOOH shown in Fig. S14. If the Cl is chemisorbed at the unsaturated Ni sites, it could yield an octahedral geometry with hexacoordinate structure, inhibited the adsorption process of hydroxyl ions and showed the site blocking effect. When the bridge OH species is replaced by Cl, extra negative charge will be generated around the Ni center, which will further lower the effective formal oxidation state. By comparing the Bader charges of Cl<sub>N</sub>-(Fe)NiOOH and Cl<sub>B</sub>-(Fe)NiOOH chloride coordination models in Table S4, we can see that Cl<sub>B</sub>-(Fe)NiOOH is in better correspondence to the FTacV experimental results. Thus, we take Cl<sub>B</sub>-(Fe)NiOOH as our target model catalyst in the following discussion. The addition of Cl may also affect the four-step OER process through the bridge OH species replaced by Cl. The structure model and the corresponding OER process is shown in Fig. 5a and b. The highest reaction energy barriers ( $\Delta G_{\max}$ ) on (Fe)NiOOH and Cl<sub>B</sub>-(Fe)NiOOH oxyhydroxide surfaces are both the OH\* deprotonation step, and the overpotentials ( $\eta$ ) increase from 0.42 V of  $\beta$ -(Fe)NiOOH to 0.66 V ( $\eta = \Delta G_{\max}/e - 1.23$ ) of Cl<sub>B</sub>-(Fe)NiOOH. This indicates the incorporation of Cl does not change the rate determining step but enhances the reaction energy barrier.

The projected densities of states (PDOS) of (Fe)NiOOH and Cl<sub>B</sub>-(Fe)NiOOH are shown in Fig. 5c. Since soft Cl-donor ligand come into being, the d<sub>xy</sub>, d<sub>yz</sub>, and d<sub>x<sup>2</sup>-y<sup>2</sup></sub> orbitals of Ni shifted to a lower energy with decreased Ni-O ligands covalency, which lead to a more negative d-band center of Ni compared to undoped ones. Therefore, the deprotonation processes of the intermediates on the metal sites are deterred, which is consistent with the reaction energy barrier diagram (Fig. 5b). Furthermore, the incorporation of Cl atoms into the lattice might generate more

negative charge states around the Ni center, and further form a lower effective formal oxidation state to bring the lagged effect. Thus, we conclude that the Cl incorporation changes the electron environment of Ni site, resulting in the larger energy barrier of the OH\* deprotonation step and lower the OER activity.

### 3.5. Effect of carbonate ions

Adding polyanions into electrolytes has proved to be an effective strategy to suppress the corrosion effects of chloride ions [58,59]. As a common intercalation ion in layered double hydroxides, carbonate has a strong affinity with transition metal hydroxide layer [60,61]. Carbonate is a weak base salt that has a low degree of hydrolysis in strong alkaline environments, resulting in little impact on the pH of the electrolyte, as can be seen in Table S5. So, we applied carbonates to undermine the negative effects of the Cl incorporation. The LSV and FtacV measurements of Ni<sub>4</sub>(OH)<sub>2</sub>/FeOOH were carried out in 1 M KOH, 1 M KOH/2 M NaCl and 1 M KOH/2 M NaCl/1 M K<sub>2</sub>CO<sub>3</sub>, respectively (Fig. 6a, b). Fig. 6a shows that the OER performance was recovered from the poison effect of Cl incorporation by adding carbonates in electrolyte. From the FtacV measurements in Fig. 6b and Fig. S15, the generation potential of high-valence Ni(IV) shifted negatively in 1 M KOH/2 M NaCl/1 M K<sub>2</sub>CO<sub>3</sub> compared with the potential in 1 M KOH/2 M NaCl. It suggests that the carbonate additive has suppressed the Cl incorporation into the electrode to some extent, which benefits the generation of high-valence Ni(IV) so as to enhance the catalytic activity. The electrocatalyst durability test was conducted in 1 M KOH/2 M

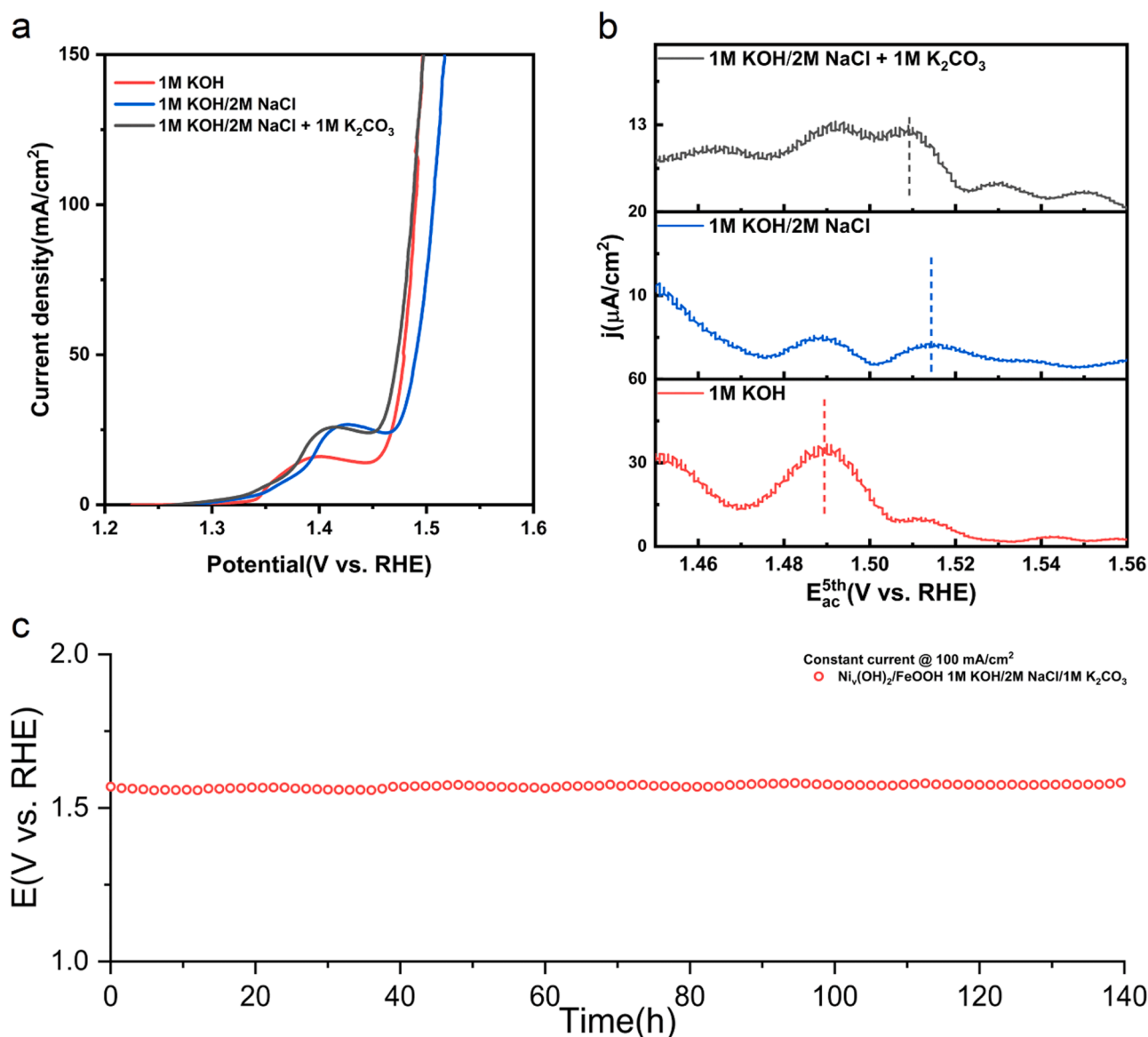


**Fig. 6.** (a) LSV curves of  $\text{Ni}_v(\text{OH})_2/\text{FeOOH}$  ( $iR$ -corrected) tested in 1 M KOH, 1 M KOH/2 M NaCl and 1 M KOH/2 M NaCl/1 M  $\text{K}_2\text{CO}_3$ . (b) 5th harmonic FTAC voltammetry components ( $f = 0.512 \text{ Hz}$ ,  $\Delta E = 80 \text{ mV}$ , scan rate  $= 0.5 \text{ mV s}^{-1}$ , positive sweep) of  $\text{Ni}_v(\text{OH})_2/\text{FeOOH}$  process III measured in different electrolytes (dash lines indicating the potential of process III). (c) Electrolysis durability test at constant current densities of  $100 \text{ mA cm}^{-2}$  in 1 M KOH/2 M NaCl/1 M  $\text{K}_2\text{CO}_3$  for a total period of 140 h.

NaCl/1 M  $\text{K}_2\text{CO}_3$  at a constant current density of  $100 \text{ mA cm}^{-2}$ . As shown in Fig. 6c, the electrode showed little performance change after working for over 140 h. The above results indicate that the additive of carbonates has significantly blocked the poison effects of  $\text{Cl}^-$  and thus enabled the robust saline water oxidation of  $\text{Ni}_v(\text{OH})_2/\text{FeOOH}$ .

#### 4. Conclusion

In this work, the  $\text{Ni}_v(\text{OH})_2/\text{FeOOH}$  catalyst was synthesized by forming FeOOH nanoparticles on the surface of  $\text{Ni}_v(\text{OH})_2$  nanosheet using a simple metal ion adsorption method, and served as a model system to elucidate the high-valence catalytic center and the deactivation effect of  $\text{Cl}^-$ . Compared with sole  $\text{Ni}_v(\text{OH})_2$  and  $\text{RuO}_2$ ,  $\text{Ni}_v(\text{OH})_2/\text{FeOOH}$  exhibits much better OER performance and the overpotential is only 262 mV for the current density of  $100 \text{ mA cm}^{-2}$ . This is due to the in-situ formation of high-valence Ni(IV) during the OER process. A surprising finding that eluded previous investigations is that adding chlorine anions in the electrolyte significantly decreased the OER

performance by increasing the generation potentials of Ni(IV). This is corroborated by theoretical calculation results that the replacement of the bridge OH- species by  $\text{Cl}^-$  restrains the formation of the high-valence Ni(IV), resulting in a largely increased energy barrier in the  $\text{OH}^*$  deprotonation step and thus the deteriorated OER activity. The addition of carbonate ions can restrain the poison effect of  $\text{Cl}^-$ , benefiting the formation of Ni(IV) at low potential to restore the OER activity of  $\text{Ni}_v(\text{OH})_2/\text{FeOOH}$  in saline water. This work highlights the importance of the high-valence Ni(IV) for OER and provides a deep understanding about the effect of chlorine anions on the OER catalysis so that it could help to design more active and stable seawater splitting catalysts.

#### CRediT authorship contribution statement

**Feng Dong:** Conduction of experiments, Investigation, Data curation, Formal analysis, Writing – original draft. **Huan Duan:** Writing – review & editing, Formal analysis. **Zedong Lin:** Writing – review & editing, Formal analysis. **Haifeng Yuan:** Data curation, Formal analysis,

Validation, Methodology. **Min Ju**: Formal analysis. **Xinjuan Du**: Data curation. **Jinqiang Gao**: Writing – review & editing, Validation. **Jun Yu**: Supervision, Funding acquisition, Writing – review & editing, Validation. **Shihe Yang**: Supervision, Writing – review & editing, Validation, Funding acquisition.

## Declaration of Competing Interest

The authors declare that they have no known competing financial interests or personal relationships that could have appeared to influence the work reported in this paper.

## Data availability

Data will be made available on request.

## Acknowledgements

This work was financially supported by National Natural Science Foundation of China (21972006), Shenzhen Science and Technology Innovation Commission (KCXFZ20201221173604012) and Shenzhen Peacock plan (KQTD2016053015544057).

## Appendix A. Supporting information

Supplementary data associated with this article can be found in the online version at [doi:10.1016/j.apcatb.2023.123242](https://doi.org/10.1016/j.apcatb.2023.123242).

## References

- [1] J. Kibsgaard, I. Chorkendorff, Considerations for the scaling-up of water splitting catalysts, *Nat. Energy* 4 (2019) 430–433, <https://doi.org/10.1038/s41560-019-0407-1>.
- [2] Z.W. Seh, J. Kibsgaard, C.F. Dickens, I.B. Chorkendorff, J.K. Nørskov, T. F. Jaramillo, Combining theory and experiment in electrocatalysis: insights into materials design, *Science* 355 (2017), <https://doi.org/10.1126/science.aad4998>.
- [3] N.T. Suen, S.F. Hung, Q. Quan, N. Zhang, Y.J. Xu, H.M. Chen, Electrocatalysis for the oxygen evolution reaction: recent development and future perspectives, *Chem. Soc. Rev.* 46 (2017) 337–365, <https://doi.org/10.1039/c6cs00328a>.
- [4] J.J. Song, C. Wei, Z.F. Huang, C.T. Liu, L. Zeng, X. Wang, Z.C.J. Xu, A review on fundamentals for designing oxygen evolution electrocatalysts, *Chem. Soc. Rev.* 49 (2020) 2196–2214, <https://doi.org/10.1039/c9cs00607a>.
- [5] J. Yu, X.J. Du, H.Z. Liu, C. Qiu, R.X. Yu, S.M. Li, J.Z. Ren, S.H. Yang, Mini review on active sites in Ce-based electrocatalysts for alkaline water splitting, *Energy Fuels* 35 (2021) 19000–19011, <https://doi.org/10.1021/acs.energyfuels.1c02087>.
- [6] J. Yu, Q. Cao, Y.B. Li, X. Long, S.H. Yang, J.K. Clark, M. Nakabayashi, N. Shibata, J. J. Delaunay, Defect-Rich NiCeO<sub>x</sub> Electrocatalyst with Ultrahigh Stability and Low Overpotential for Water Oxidation, *ACS Catal.* 9 (2019) 1605–1611, <https://doi.org/10.1021/acscatal.9b00191>.
- [7] G. Wang, C. Jin, G. Zhang, L. Qian, X. Chen, J. Tan, W. Wang, J. Yin, X. Liu, H. Zhou, Surface self-reconstructed amorphous/crystalline hybrid iron disulfide for high-efficiency water oxidation electrocatalysis, *Dalton Trans.* Int. J. Inorg. Chem. 5 (2021) 6333–6342, <https://doi.org/10.1039/d1dt00730k>.
- [8] G. Wang, C. Wang, L. Zhao, F. Qiao, X. Zhang, H. Wang, W. Wang, J. Yin, H. Zhou, X. Liu, Completely reconfigured Fe<sub>1-x</sub>S/C ultra-thin nanocomposite lamellar structure for highly efficient oxygen evolution, *Fuel (Guildf.)* 341 (2023), 127686, <https://doi.org/10.1016/j.fuel.2023.127686>.
- [9] H. Liu, J. Yu, J. Lin, B. Feng, M. Sun, C. Qiu, K. Qian, Z. Si, B. Huang, J.-J. Delaunay, Y. Ikuhara, S. Yang, CeO<sub>2</sub> supported high-valence Fe oxide for highly active and stable water oxidation, *EES Catal.* (2023), <https://doi.org/10.1039/D3EY00113J>.
- [10] H. Yang, C.L. Dong, H.M. Wang, R.J. Qi, L.Q. Gong, Y.R. Lu, C.H. He, S.H. Chen, B. You, H.F. Liu, J.L. Yao, X.L. Jiang, X.P. Guo, B.Y. Xia, Constructing nickel-iron oxyhydroxides integrated with iron oxides by microorganism corrosion for oxygen evolution, *Proc. Natl. Acad. Sci. USA* 119 (2022), <https://doi.org/10.1073/pnas.2202812119>.
- [11] Z.Y. He, J. Zhang, Z.H. Gong, H. Lei, D. Zhou, N.A. Zhang, W.J. Mai, S.J. Zhao, Y. Chen, Activating lattice oxygen in NiFe-based (oxy)hydroxide for water electrolysis, *Nat. Commun.* 13 (2022), <https://doi.org/10.1038/s41467-022-29875-4>.
- [12] Y. Wang, Y.Z. Zhao, L. Liu, W.J. Qin, S.J. Liu, J.P. Tu, Y.P. Qin, J.F. Liu, H.Y. Wu, D. Y. Zhang, A.M. Chu, B.R. Jia, X.H. Qu, M.L. Qin, Mesoporous Single Crystals with Fe-Rich Skin for Ultralow Overpotential in Oxygen Evolution Catalysis, *Adv. Mater.* 34 (2022), <https://doi.org/10.1002/adma.202200088>.
- [13] F. Dionigi, J. Zhu, Z.H. Zeng, T. Merzdorf, H. Sarodnik, M. Gliech, L.J. Pan, W.X. Li, J. Greeley, P. Strasser, Intrinsic electrocatalytic activity for oxygen evolution of crystalline 3d-transition metal layered double hydroxides, *Angew. Chem. -Int. Ed.* 60 (2021) 14446–14457, <https://doi.org/10.1002/anie.202100631>.
- [14] F. Wang, X. Sun, Y. Wang, H. Zhou, J. Yin, X. Zhang, Metallized Ni(OH)<sub>2</sub>-NiO/FeOOH on Ni foam as a highly effective water oxidation catalyst prepared by surface treatment: oxidation–corrosion equilibrium, *ACS Appl. Energy Mater.* 4 (2021) 5599–5605, <https://doi.org/10.1021/acsaem.1c00384>.
- [15] J. Yin, F. Di, J. Guo, K. Zhang, W. Xu, Y. Wang, S. Shi, N. Chai, C. Chu, J. Wei, W. Li, X. Shao, X. Pu, D. Zhang, X. Ren, J. Wang, J. Zhao, X. Zhang, X. Wei, F. Wang, H. Zhou, Tuning Ni-Foam into NiOOH/FeOOH Heterostructures toward Superior Water Oxidation Catalyst via Three-Step Strategy, *ACS Omega* 3 (2018) 11009–11017, <https://doi.org/10.1021/acsomega.8b01143>.
- [16] L. Trotochaud, S.L. Young, J.K. Ranney, S.W. Boettcher, Nickel-iron oxyhydroxide oxygen-evolution electrocatalysts: the role of intentional and incidental iron incorporation, *J. Am. Chem. Soc.* 136 (2014) 6744–6753, <https://doi.org/10.1021/ja502379c>.
- [17] M. Gorlin, J.F. de Araujo, H. Schmies, D. Bernsmeier, S. Dresp, M. Gliech, Z. Jusys, P. Chernev, R. Kraehnert, H. Dau, P. Strasser, Tracking catalyst redox states and reaction dynamics in Ni-Fe oxyhydroxide oxygen evolution reaction electrocatalysts: the role of catalyst support and electrolyte pH, *J. Am. Chem. Soc.* 139 (2017) 2070–2082, <https://doi.org/10.1021/jacs.6b12250>.
- [18] D.K. Bediako, B. Lassalle-Kaiser, Y. Surendranath, J. Yano, V.K. Yachandra, D. G. Nocera, Structure-activity correlations in a nickel-borate oxygen evolution catalyst, *J. Am. Chem. Soc.* 134 (2012) 6801–6809, <https://doi.org/10.1021/ja301018q>.
- [19] D.N. Wang, J.G. Zhou, Y.F. Hu, J.L. Yang, N. Han, Y.G. Li, T.K. Sham, In situ X-ray absorption near-edge structure study of advanced NiFe(OH)(x) electrocatalyst on carbon paper for water oxidation, *J. Phys. Chem. C* 119 (2015) 19573–19583, <https://doi.org/10.1021/acs.jpcc.5b02685>.
- [20] W.E. Ogrady, K.I. Pandya, K.E. Swider, D.A. Corrigan, In situ x-ray absorption near-edge structure evidence for quadrivalent nickel in nickel battery electrodes, *J. Electrochem. Soc.* 143 (1996) 1613–1616, <https://doi.org/10.1149/1.1836687>.
- [21] P. Acharya, R.H. Manso, A.S. Hoffman, S.I.P. Bakovic, L. Kekedy-Nagy, S.R. Bare, J. Y. Chen, L.F. Greenlee, Fe Coordination Environment, Fe-Incorporated Ni(OH)<sub>2</sub>(2) Phase, and Metallic Core Are Key Structural Components to Active and Stable Nanoparticle Catalysts for the Oxygen Evolution Reaction, *ACS Catal.* 12 (2022) 1992–2008, <https://doi.org/10.1021/acscatal.1c04881>.
- [22] J.X. Kang, X.Y. Qiu, Q. Hu, J. Zhong, X. Gao, R. Huang, C.Z. Wan, L.M. Liu, X. F. Duan, L. Guo, Valence oscillation and dynamic active sites in monolayer NiCo hydroxides for water oxidation, *Nat. Catal.* 4 (2021) 1050–1058, <https://doi.org/10.1038/s41929-021-00715-w>.
- [23] J. Yu, J. Wang, X. Long, L. Chen, Q. Cao, J. Wang, C. Qiu, J. Lim, S.H. Yang, Formation of FeOOH nanosheets induces substitutional doping of CeO<sub>2-x</sub> with high-valence Ni for efficient water oxidation, *Adv. Energy Mater.* 11 (2021), <https://doi.org/10.1002/aenm.202002731>.
- [24] G. Chen, Y.P. Zhu, H.M. Chen, Z.W. Hu, S.F. Hung, N.N. Ma, J. Dai, H.J. Lin, C. T. Chen, W. Zhou, Z.P. Shao, An amorphous nickel-iron-based electrocatalyst with unusual local structures for ultrafast oxygen evolution reaction, *Adv. Mater.* 31 (2019), <https://doi.org/10.1002/adma.201900883>.
- [25] J. Zhang, A.M. Bond, Theoretical studies of large amplitude alternating current voltammetry for a reversible surface-confined electron transfer process coupled to a pseudo first-order electrocatalytic process, *J. Electroanal. Chem.* 600 (2007) 23–34, <https://doi.org/10.1016/j.jelechem.2006.02.023>.
- [26] Y. Zhang, A.N. Simonov, J. Zhang, A.M. Bond, Fourier transformed alternating current voltammetry in electromaterials research: direct visualisation of important underlying electron transfer processes, *Curr. Opin. Electrochem.* 10 (2018) 72–81, <https://doi.org/10.1016/j.coelec.2018.04.016>.
- [27] A.A. Sher, A.M. Bond, D.J. Gavaghan, K. Harriman, S.W. Feldberg, M.W. Duffy, S. X. Guo, J. Zhang, Resistance, capacitance, and electrode kinetic effects in Fourier-transformed large-amplitude sinusoidal voltammetry: Emergence of powerful and intuitively obvious tools for recognition of patterns of behavior, *Anal. Chem.* 76 (2004) 6214–6228, <https://doi.org/10.1021/ac0495337>.
- [28] Y.P. Liu, S.X. Guo, L. Ding, C.A. Ohlin, A.M. Bond, J. Zhang, Lindqvist polyoxoniobate ion-assisted electrodeposition of cobalt and nickel water oxidation catalysts, *ACS Appl. Mater. Interfaces* 7 (2015) 16632–16644, <https://doi.org/10.1021/acsaami.5b04219>.
- [29] S.A. Bonke, A.M. Bond, L. Spiccia, A.N. Simonov, Parameterization of water electrooxidation catalyzed by metal oxides using fourier transformed alternating current voltammetry, *J. Am. Chem. Soc.* 138 (2016) 16095–16104, <https://doi.org/10.1021/jacs.6b10304>.
- [30] J.N. Hausmann, R. Schloegl, P.W. Menezes, M. Driess, Is direct seawater splitting economically meaningful? *Energy Environ. Sci.* 14 (2021) 3679–3685, <https://doi.org/10.1039/d0ee03659e>.
- [31] M.A. Khan, T. Al-Attas, S. Roy, M.M. Rahman, N. Ghaffour, V. Thangadurai, S. Larter, J. Hu, P.M. Ajayan, M.G. Kibria, Seawater electrolysis for hydrogen production: a solution looking for a problem? *Energy Environ. Sci.* 14 (2021) 4831–4839, <https://doi.org/10.1039/D1EE00870F>.
- [32] F. Dionigi, T. Reier, S. Pawolek, M. Gliech, P. Strasser, Design Criteria, Operating Conditions, and Nickel-Iron Hydroxide Catalyst Materials for Selective Seawater Electrolysis, *Chemsuschem* 9 (2016) 962–972, <https://doi.org/10.1002/cssc.201501581>.
- [33] S. Dresp, F. Dionigi, S. Loos, J.F. de Araujo, C. Spöerl, M. Gliech, H. Dau, P. Strasser, Direct electrolytic splitting of seawater: activity, selectivity, degradation, and recovery studied from the molecular catalyst structure to the electrolyzer cell level, *Adv. Energy Mater.* 8 (2018), <https://doi.org/10.1002/aenm.201800338>.

- [34] L. Wu, L. Yu, F. Zhang, B. McElhenny, D. Luo, A. Karim, S. Chen, Z. Ren, Heterogeneous Bimetallic Phosphide Ni<sub>2</sub>P-Fe<sub>2</sub>P as an Efficient Bifunctional Catalyst for Water/Seawater Splitting, *Adv. Funct. Mater.* 31 (2021), 2006484, <https://doi.org/10.1002/adfm.202006484>.
- [35] Y.S. Xie, Z. Wang, M. Ju, X. Long, S.H. Yang, Dispersing transition metal vacancies in layered double hydroxides by ionic reductive complexation extraction for efficient water oxidation, *Chem. Sci.* 10 (2019) 8354–8359, <https://doi.org/10.1039/c9sc02723h>.
- [36] G. Kresse, J. Furthmüller, Efficiency of ab-initio total energy calculations for metals and semiconductors using a plane-wave basis set, *Comput. Mater. Sci.* 6 (1996) 15–50, [https://doi.org/10.1016/0927-0256\(96\)00008-0](https://doi.org/10.1016/0927-0256(96)00008-0).
- [37] G. Kresse, J. Furthmüller, Efficient iterative schemes for ab initio total-energy calculations using a plane-wave basis set, *Phys. Rev. B* 54 (1996) 11169–11186, <https://doi.org/10.1103/PhysRevB.54.11169>.
- [38] J.P. Perdew, K. Burke, M. Ernzerhof, Generalized Gradient Approximation Made Simple [Phys. Rev. Lett. 77, 3865 (1996)], 1396–1396, *Phys. Rev. Lett.* 78 (1997), <https://doi.org/10.1103/PhysRevLett.78.1396>.
- [39] P.E. Blöchl, Projector augmented-wave method, *Phys. Rev. B* 50 (1994) 17953–17979, <https://doi.org/10.1103/PhysRevB.50.17953>.
- [40] D. Friebe, M.W. Louie, M. Bajdich, K.E. Sanwald, Y. Cai, A.M. Wise, M.J. Cheng, D. Sokaras, T.C. Weng, R. Alonso-Mori, R.C. Davis, J.R. Bargar, J.K. Nørskov, A. Nilsson, A.T. Bell, Identification of Highly Active Fe Sites in (Ni,Fe)OOH for Electrocatalytic Water Splitting, *J. Am. Chem. Soc.* 137 (2015) 1305–1313, <https://doi.org/10.1021/ja511559d>.
- [41] S. Grimme, S. Ehrlich, L. Goerigk, Effect of the damping function in dispersion corrected density functional theory, *J. Comput. Chem.* 32 (2011) 1456–1465, <https://doi.org/10.1002/jcc.21759>.
- [42] H.J. Monkhorst, J.D. Pack, Special points for brillouin-zone integrations, *Phys. Rev. B* 13 (1976) 5188–5192, <https://doi.org/10.1103/PhysRevB.13.5188>.
- [43] J.K. Nørskov, J. Rossmeisl, A. Logadottir, L. Lindqvist, J.R. Kitchin, T. Bligaard, H. Jonsson, Origin of the overpotential for oxygen reduction at a fuel-cell cathode, *J. Phys. Chem. B* 108 (2004) 17886–17892, <https://doi.org/10.1021/jp047349j>.
- [44] H. Bode, K. Dehmelt, J. Witte, Zur kenntnis der nickelhydroxidelektrode—I. Über das nickel (II)-hydroxidhydrat, *Electrochim. Acta* 11 (1966) 1079–1087, [https://doi.org/10.1016/0013-4686\(66\)80045-2](https://doi.org/10.1016/0013-4686(66)80045-2).
- [45] H. Liu, H. Duan, J. Yu, C. Qiu, R. Yu, J. Gao, S. Li, X. Du, Z. Si, S. Yang, Strong Electron Coupling Effect at the CoO/CeO<sub>2</sub> Interface Enables Efficient Oxygen Evolution Reaction, *ACS Mater. Lett.* 4 (2022) 2572–2578, <https://doi.org/10.1021/acsmaterialslett.2c00802>.
- [46] Q.Q. Li, Z.C. Zeng, X.L. Sun, F. Luo, Y.P. Du, CeO<sub>2</sub> with diverse morphologies-supported IrOx nanocatalysts for efficient oxygen evolution reaction - Commemorating the 100th anniversary of the birth of Academician Guangxian Xu, *J. Rare Earths* 39 (2021) 357–363, <https://doi.org/10.1016/j.jre.2020.12.020>.
- [47] X.J. Zhao, Y. Chang, X.L. He, H.Q. Zhang, J.C. Jia, M.L. Jia, Understanding ultra-dispersed CeOx modified iridium clusters as bifunctional electrocatalyst for high-efficiency water splitting in acid electrolytes, *J. Rare Earths* 41 (2023) 208–214, <https://doi.org/10.1016/j.jre.2022.01.013>.
- [48] S.M. Li, H. Duan, J. Yu, C. Qiu, R.X. Yu, Y.P. Chen, Y.P. Fang, X. Cai, S.H. Yang, Cu vacancy induced product switching from formate to CO for CO<sub>2</sub> reduction on copper sulfide, *Acs Catal.* 12 (2022) 9074–9082, <https://doi.org/10.1021/acscatal.2c01750>.
- [49] C. Qiu, K. Qian, J. Yu, M.Z. Sun, S.F. Cao, J.Q. Gao, R.X. Yu, L.Z. Fang, Y.W. Yao, X. Q. Lu, T. Li, B.L. Huang, S.H. Yang, MOF-Transformed In<sub>2</sub>O<sub>3</sub>-x@C Nanocorn Electrocatalyst for Efficient CO<sub>2</sub> Reduction to HCOOH, *Nano-Micro Lett.* 14 (2022), <https://doi.org/10.1007/s40820-022-00913-6>.
- [50] R.D.L. Smith, R.S. Sherbo, K.E. Dettelbach, C.P. Berlinguette, On how experimental conditions affect the electrochemical response of disordered nickel oxyhydroxide films, *Chem. Mater.* 28 (2016) 5635–5642, <https://doi.org/10.1021/acs.chemmater.6b01420>.
- [51] M. Yoshida, Y. Mitsutomi, T. Mineo, M. Nagasaka, H. Yuzawa, N. Kosugi, H. Kondoh, Direct observation of active nickel oxide cluster in nickel borate electrocatalyst for water oxidation by in situ O K-Edge X-ray absorption spectroscopy, *J. Phys. Chem. C* 119 (2015) 19279–19286, <https://doi.org/10.1021/acs.jpcc.5b06102>.
- [52] M. Alsabet, M. Grden, G. Jerkiewicz, Electrochemical Growth of Surface Oxides on Nickel. Part 3: Formation of beta-NiOOH in Relation to the Polarization Potential, Polarization Time, and Temperature, *Electrocatalysis* 6 (2015) 60–71, <https://doi.org/10.1007/s12678-014-0214-1>.
- [53] B.S. Yeo, A.T. Bell, In situ raman study of nickel oxide and gold-supported nickel oxide catalysts for the electrochemical evolution of oxygen, *J. Phys. Chem. C* 116 (2012) 8394–8400, <https://doi.org/10.1021/jp3007415>.
- [54] M.K. Bates, Q.Y. Jia, H. Doan, W.T. Liang, S. Mukerjee, Charge-Transfer Effects in Ni-Fe and Ni-Fe-Co Mixed-Metal Oxides for the Alkaline Oxygen Evolution Reaction, *Acs Catal.* 6 (2016) 155–161, <https://doi.org/10.1021/acscatal.5b01481>.
- [55] R. Chen, S.F. Hung, D. Zhou, J. Gao, C. Yang, H. Tao, H.B. Yang, L. Zhang, L. Zhang, Q. Xiong, H.M. Chen, B. Liu, Layered Structure Causes Bulk NiFe Layered Double Hydroxide Unstable in Alkaline Oxygen Evolution Reaction (-n/a), *Adv. Mater. (Weinh. )* 31 (2019), e1903909, <https://doi.org/10.1002/adma.201903909>.
- [56] F. Dionigi, T. Reier, Z. Pawolek, M. Glicke, P. Strasser, Design criteria, operating conditions, and nickel-iron hydroxide catalyst materials for selective seawater electrolysis, *ChemSusChem* 9 (2016) 962–972, <https://doi.org/10.1002/cssc.201501581>.
- [57] J.M.P. Martirez, E.A. Carter, Unraveling oxygen evolution on iron-doped beta-nickel oxyhydroxide: the key role of highly active molecular-like sites, *J. Am. Chem. Soc.* 141 (2019) 693–705, <https://doi.org/10.1021/jacs.8b12386>.
- [58] T. Ma, W. Xu, B. Li, X. Chen, J. Zhao, S. Wan, K. Jiang, S. Zhang, Z. Wang, Z. Tian, Z. Lu, L. Chen, The critical role of additive sulfate for stable alkaline seawater oxidation on nickel-based electrodes, *Angew. Chem. -Int. Ed.* 60 (2021) 22740–22744, <https://doi.org/10.1002/anie.202110355>.
- [59] M. Yu, J. Li, F. Liu, J. Liu, W. Xu, H. Hu, X. Chen, W. Wang, F. Cheng, Anionic formulation of electrolyte additive towards stable electrocatalytic oxygen evolution in seawater splitting, *J. Energy Chem.* 72 (2022) 361–369, <https://doi.org/10.1016/j.jechem.2022.04.004>.
- [60] X. Wang, L. Li, Z.-H. Xie, G. Yu, Duplex coating combining layered double hydroxide and 8-quinolinol layers on Mg alloy for corrosion protection, *Electrochim. Acta* 283 (2018) 1845–1857, <https://doi.org/10.1016/j.electacta.2018.07.113>.
- [61] B.M. Hunter, W. Hieringer, J.R. Winkler, H.B. Gray, A.M. Müller, Effect of interlayer anions on [NiFe]-LDH nanosheet water oxidation activity, *Energy Environ. Sci.* 9 (2016) 1734–1743, <https://doi.org/10.1039/C6EE00377J>.